ADVANCED MATERIALS
www.advmat.de

Large and Ultrastable All-Inorganic $CsPbBr_3$ Monocrystalline Films: Low-Temperature Growth and Application for High-Performance Photodetectors

*Zheng Yang, Qian Xu, Xiandi Wang, Junfeng Lu, Hui Wang, Fangtao Li, Li Zhang, Guofeng Hu, and Caofeng Pan**

Stability is a key problem that hinders the practical application of lead halide perovskite. Therefore, all-inorganic perovskite $CsPbX_3$ monocrystalline films are urgently needed to fabricate photoelectric devices. Herein, a low-temperature and substrate-independent growth method is demonstrated to grow millimeter-level inorganic perovskite monocrystalline thin films. These films present good optical and electrical properties comparable to bulk ones. What is more, they exhibit excellent long-term stability toward humidity and thermal treatment. The as-grown $CsPbBr_3$ monocrystalline films are then fabricated into photodetectors with high photodetection performance. These results demonstrate that the $CsPbBr_3$ monocrystalline films have potential in fabricating high-performance optoelectronic devices.

Recently, lead halide perovskites have aroused tremendous interests in various optoelectronic applications such as solar cells,[1–6] light-emitting diodes (LEDs),[7–11] lasers,[12–17] and photodetectors.[18–22] Compared with other commonly used semiconductors,[23–29] perovskites present excellent photoelectric properties such as long-range charge transport and efficient charge collection, long carrier diffusion length, broad chemical tunability, and high balanced hole and electron mobility.[30–32] Although the organic–inorganic hybrid perovskites have been deeply studied, it is worth noting that they suffer from low thermal stability and poor antiaqueous solubility, which hinder their practical applications. All-inorganic perovskites $CsPbX_3$ (X = Cl, Br, I) which have much higher chemical stability than the hybrid ones have been considered a class of advanced optoelectronic materials.[33–35] Large perovskite single crystals show significantly higher carrier mobility, longer diffusion length, and carrier lifetime than the small ones especially nanoforms. However, compared with the hybrids, much fewer studies have developed approaches for growing large-scale inorganic perovskite single crystals.[36–39] At present, most of the $CsPbX_3$ perovskites are in nanoscale or polycrystalline forms. Besides, the common synthesis methods for $CsPbX_3$ monocrystalline perovskite such as Bridgman technique, hot-injection route, and ligand-mediated reprecipitation rely on high temperature and need the addition of ligands. Furthermore, compared with the bulk counterparts, the monocrystalline thin films are more suitable for device fabrication.[40] Up to now, the growth methods for hybrid perovskites monocrystalline thin films have been extensively demonstrated,[40–43] however, the fabrication of large all-inorganic perovskite monocrystalline films is rarely mentioned and highly worth studying to boost device performance.

Herein, we present a low-temperature and substrate-independent growth method for ultrastable millimeter-size all-inorganic perovskite monocrystalline films. The size can be well controlled by varying the growth time. The optical and electrical properties of monocrystalline films, such as steady-state fluorescence, carrier concentration and mobility, and fluorescent lifetime are comprehensively demonstrated. The halogen components and proportion can be modulated via a vapor-phase halide-exchange method and thus tuning the optical properties such as color and bandgaps. Besides, these films present excellent long-term stability toward humidity and thermal treatment, which is vital for practical applications. Then the as-grown $CsPbBr_3$ monocrystalline films were fabricated into photodetectors which exhibit high light detecting performance such as fast response and recovery, high external quantum efficiency (EQE), and long-term stability. These $CsPbBr_3$ monocrystalline films have potential applications in other optoelectronic applications such as solar cells and LEDs.

Z. Yang, Q. Xu, Dr. X. D. Wang, Dr. J. F. Lu, F. T. Li, L. Zhang, Dr. G. F. Hu, Prof. C. F. Pan
CAS Center for Excellence in Nanoscience
Beijing Key Laboratory of Micro-Nano Energy and Sensor
Beijing Institute of Nanoenergy and Nanosystems
Chinese Academy of Sciences
Beijing 100083, P. R. China
E-mail: cfpan@binn.cas.cn

Z. Yang, Q. Xu, Dr. X. D. Wang, Dr. J. F. Lu, Dr. G. F. Hu, Prof. C. F. Pan
School of Nanoscience and Technology
University of Chinese Academy of Sciences
Beijing 100049, P. R. China

Prof. H. Wang
Key Laboratory of Aerospace Materials and Performance
(Ministry of Education)
School of Materials Science and Engineering
Beihang University
Beijing 100191, P. R. China

The ORCID identification number(s) for the author(s) of this article can be found under https://doi.org/10.1002/adma.201802110.

DOI: 10.1002/adma.201802110

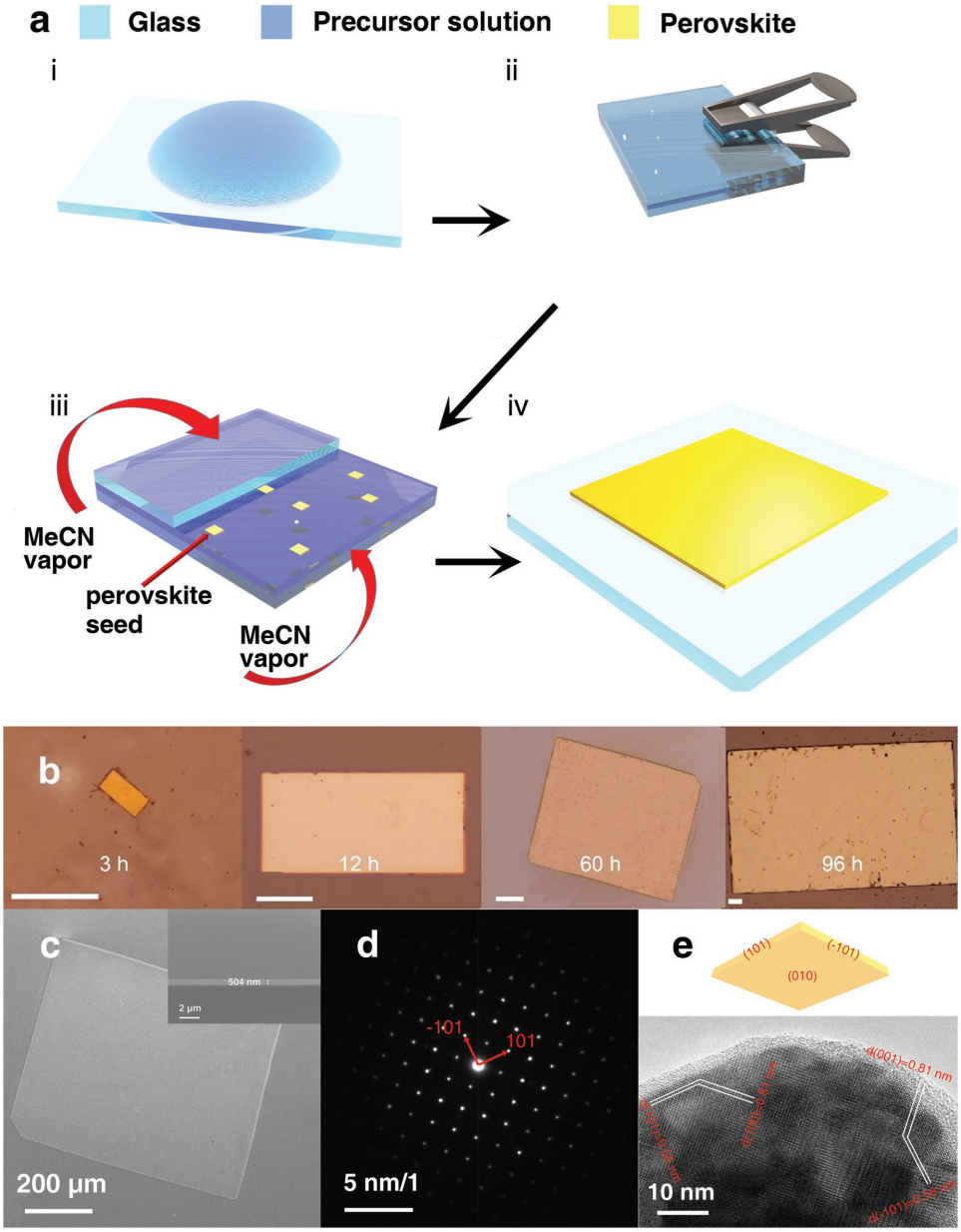

Figure 1. a) Schematic diagram for growth of $CsPbBr_3$ monocrystalline films. b) Optical images of $CsPbBr_3$ monocrystalline films on the glass substrate for four different growing time (scale bar: 100 μm). c) The top-view and side-view (inset) SEM image of the $CsPbBr_3$ monocrystalline film. d) SAED pattern of the $CsPbBr_3$ monocrystalline film along the [001] zone axis. e) HRTEM image showing the orthogonal structure (inset: indices of three crystal face).

A space-limited antisolvent vapor-assisted crystallization growth is demonstrated to achieve the fabrication of large-area inorganic perovskite monocrystalline thin films. Schematic illustration of the inorganic perovskite monocrystalline thin films growth is shown in **Figure 1**a i–iv. A stock solution (50 μL) of equimolar CsBr and $PbBr_2$ in dimethyl sulfoxide (DMSO) was spread on a 2.5 × 2.5 cm hydrophilic substrate. The solution preparation procedure is described in the Experimental Section. Then another octadecyltrichlorosilane (OTS) treated hydrophobic substrate was brought into contact with the DMSO solution and two clean flat substrates were clipped together. A pressure was applied uniformly on the two substrates. The bubbles in the solution were eliminated by a few seconds vacuum pumping. Then they were placed in a sealed glass beaker which contained acetonitrile (CH_3CN). The glass beaker can be put in a 40 °C oven to boost the growth rate. Since CH_3CN is a poor solvent for $CsPbBr_3$ and its dielectric constant is close to DMSO,[39] therefore, slow diffusion of CH_3CN vapor into DMSO solution would induce the nucleation of $CsPbBr_3$ (Figure 1a iii) rather than CsBr-rich Cs_4PbBr_6 or $PbBr_2$-rich $CsPb_2Br_5$ and subsequent growth of $CsPbBr_3$ monocrystalline films between two clipped substrates.

The optical images in Figure 1b show the growth procedure of the $CsPbBr_3$ monocrystalline films. By refreshing the

precursor solution via removing the old solvent and injecting the new solution after a certain time (usually 12 h) and extending growth periods, the films can grow larger. After the growth of 96 h, mm level monocrystalline films without grain boundaries and defects have been in situ grown on the substrate, which is also shown in the photograph (Figure 1d). As shown in the top-view scanning electron microscopy (SEM) image (Figure 1c) and optical image (Figure 1b), the $CsPbBr_3$ film which had grown for 12 h with a size of ≈200 µm are homogeneous and containing no grain boundaries and voids, proving their monocrystalline structure. Energy-dispersive X-ray spectroscopy (EDS) analysis was conducted to confirm the chemical composition (Figure S1b–d, Supporting Information). The elemental mapping results indicate that Cs, Pb, and Br elements are uniformly distributed in the film and the atomic ratio of 0.95:1:2.89 accords with the $CsPbBr_3$ stoichiometry in Figure S2 (Supporting Information). The optical image and top-view SEM image (Figure 1b,c) prove that the film also show angled facets and smooth surfaces. The SEM of side view (inset in Figure 1c) and height profile image (Figure S3, Supporting Information) evidenced the thicknesses of perovskite monocrystalline films were very uniform. The thickness of the perovskite films could be easily regulated by changing the pressure imposed on the clipped substrates. Figure S4 (Supporting Information) shows the relationship between the film thickness and the applied pressure. With the increase of the applied pressure, the film thickness nonlinearly decreased. For a pressure of 200 kPa, the thickness is about 500 nm (inset of Figure 1c). These perovskite monocrystalline films can also directly grow on a variety of flat substrates such as poly(ethylene naphthalate) (PEN), SiO_2/Si, and silicon wafer (Figure S5a–c, Supporting Information), which can widen the range of their applications. The photograph of the $CsPbBr_3$ monocrystalline films grown on the glass substrate with size of mm level is shown in Figure S6 (Supporting Information). The monocrystalline $CsPbBr_3$ films were also characterized with transmission electron microscope (TEM) in Figure S7 (Supporting Information). Figure 1d shows the selected area electron diffraction (SAED) pattern of single-crystal $CsPbBr_3$ film indexed to the [001] zone axis of orthorhombic crystal structure, which is agreed with the previous reports.[17,44] The orthotropic lattice planes with distance of 0.58, 0.58, 0.81, and 0.81 nm are observed under the high-resolution TEM (Figure 1e), which can be attributed to the (101), (–101), (100), and (001) planes, respectively. The black particles in TEM are Pb crystals caused by high-voltage electron beam irradiation.[45] So, three indices of crystal face are (–101), (101), and (010), respectively.

The X-ray diffraction (XRD) pattern of our $CsPbBr_3$ single-crystal films on the glass substrate showed the typical orthorhombic crystalline structure of $CsPbBr_3$ (**Figure 2**a). Two distinct characteristic peaks at 15.3° and 31.0° shown in XRD spectrum are assigned to the (020) and (040) crystal planes of the $CsPbBr_3$, respectively, indicating that the film's exposed face is (010) crystal plane, which is in accordance with the SAED result. Clear splitting of (020)/(101) as well as (040)/(202) peaks in the spectrum also demonstrates the films have an orthorhombic crystal structure. The good crystallinity of the films is further confirmed by a full width at half maximum (FWHM) of 0.13°. The peaks of steady-state photoluminescence PL spectrum (blue curve) and absorption spectrum (red curve) of the $CsPbBr_3$ perovskite monocrystalline films are shown in Figure 2b. The PL peak at about 600 nm derived from surface defects is not identified, indicating a high crystalline characteristic. The absorption spectrum of the $CsPbBr_3$ monocrystalline films has the absorption onset of 561 nm and the corresponding optical bandgap is calculated as 2.2 eV (Figure 2c). As shown in Figure 2d, the decay curve of transient state PL for $CsPbBr_3$ with an excitation light of 370 nm was fitted via two-exponential method showing two time components of a fast (1.29 ns) and a slow (7.56 ns) dynamics. The two different-scales' carrier lifetimes are regarded as the surface and bulk recombination, respectively.[38] To evaluate the carrier transport properties of the $CsPbBr_3$ monocrystalline films, the space charge limited current method was introduced. Since $CsPbBr_3$ crystal is a p-type semiconductor,[46] both hole-only (using Ti/Au as electrodes, as shown in Figure 2e) and electron-only devices (using Au electrodes, as shown in Figure 2f) were fabricated. The film thickness used here is about 5 µm. The dark *I*–*V* curves were measured to derive the electrical properties of the $CsPbBr_3$ films. There exist three regions in the *I*–*V* curves, linear ohmic region (blue), trap-filled region (green), and trap-free Child's regime (orange). From the curves, the trap-filled limit voltage (V_{TFL}) can be deduced. Then the carrier mobility (μ), trap density (n_{trap}), and the carrier diffusion length (L) can be calculated using Equations (1), (2), and (3) according to the published report,[6] where ε, ε_0, d, J_d, and k_B denote the relative dielectric constant, vacuum permittivity, film thickness, current density, and Boltzmann constant, respectively

$$n_{trap} = \frac{2V_{TFL}\varepsilon_0\varepsilon}{ed^2} \tag{1}$$

$$\mu = \frac{8J_D d^3}{9\varepsilon\varepsilon_0 {V_b}^2} \tag{2}$$

$$L = \sqrt{\frac{k_B T}{q}\mu\tau} \tag{3}$$

As a consequence, the electron mobility (μ_e) and trap density (n_{trap}) were estimated as 910 $cm^2\ s^{-1}\ V^{-1}$ and $1.27 \times 10^{10}\ cm^{-3}$, and the hole mobility (μ_h) and trap density (n_{trap}) were estimated as 1770 $cm^2\ s^{-1}\ V^{-1}$ and $1.82 \times 10^{10}\ cm^{-3}$, respectively. As a result, the $CsPbBr_3$ films reveal p-type conduction, which accords with our speculation. The electron and hole diffusion length of the $CsPbBr_3$ films are 5.9 and 4.2 µm. We compare the optical and electrical properties of our $CsPbBr_3$ film with other typical $MAPbBr_3$ monocrystalline films or $CsPbBr_3$ crystals and the relevant data are listed in **Table 1**. The trap density, diffusion length, and mobility-lifetime product of our $CsPbBr_3$ film and other typical $CsPbBr_3$ bulk crystals or $MAPbBr_3$ films are in the same order of magnitude, implying the comparable crystal quality. The mobility of our films is a little less than the Bridgman method obtained $CsPbBr_3$ bulk crystal[38] and higher than the $MAPbBr_3$ films. The lifetime of 7.56 ns is relatively lower than the $MAPbBr_3$ films but consistent with $CsPbBr_3$ bulk crystal.[38] This may be attributed to increased surface traps in $CsPbBr_3$. The resistivity of the $CsPbBr_3$ monocrystalline film is about 0.21 GΩ cm, which is comparable to high-quality $CsPbBr_3$ bulk crystal.[37] With the continued increase of

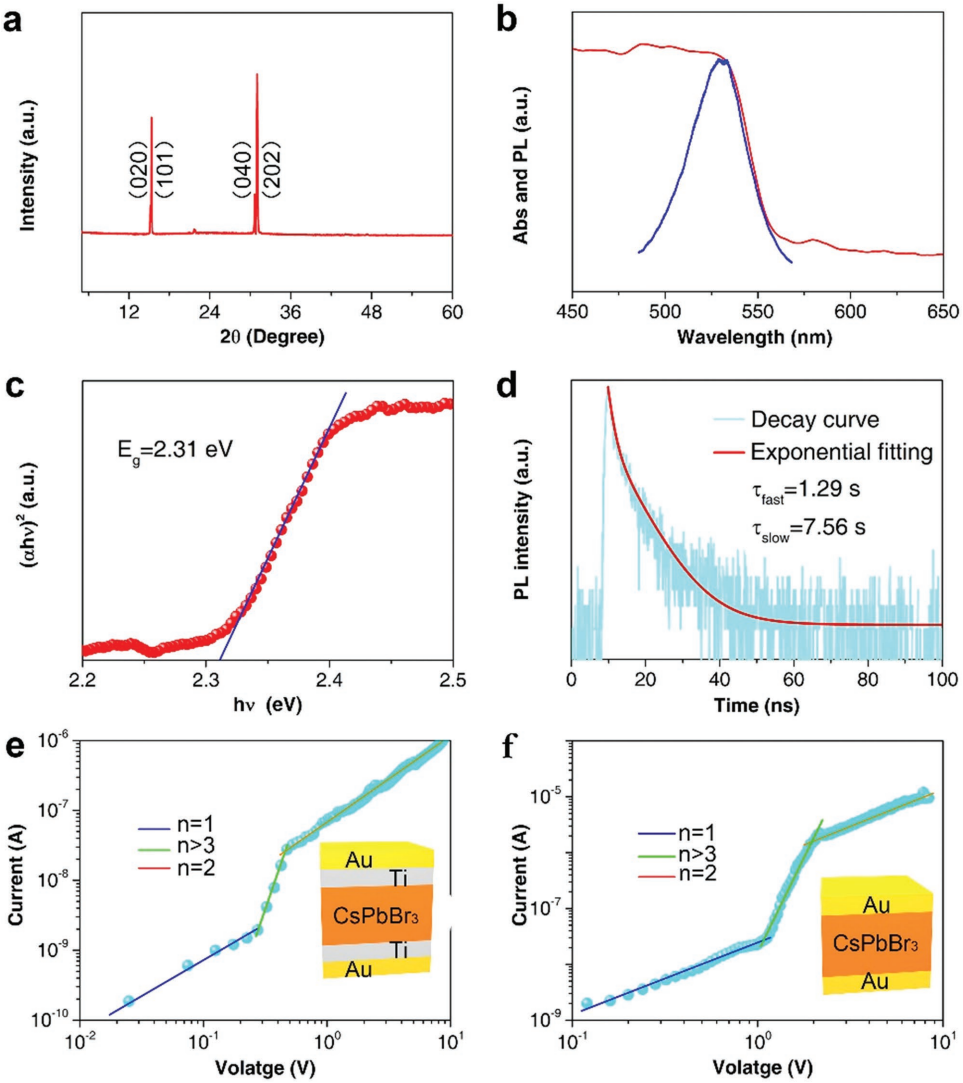

Figure 2. a) The XRD spectrum of the $CsPbBr_3$ film which shows the orthorhombic phase. b)The PL (blue) and absorption (red) spectra of the $CsPbBr_3$ film. c) Optical bandgap of the $CsPbBr_3$ film. d) The PL decay profiles of $CsPbBr_3$ monocrystalline monitored around 530 nm excited by a 325 nm laser. The *I–V* characteristic for e) a hole-only device and f) an electron-only device, where blue, green, and orange lines are identified as linear Ohmic ($n = 1$), trap-filled ($n > 3$), and trap-free Child's regime ($n = 2$), respectively. Insets are the device structures.

the voltage, the current increases. However, when the voltage reaches 82 V, the current abruptly oversteps the limit of 4200 source-measure unit (Figure S8, Supporting Information). So the breakdown voltage is ≈82 V.

Unlike organic–inorganic hybrid perovskites, it is difficult to obtain $CsPbCl_3$, $CsPbI_3$ monocrystalline films directly. A vapor-phase halide-exchange method could be used to convert $CsPbBr_3$ into $CsPbX_3$ (X = Cl, Br, I) using hydrogen halide vapors and modulate the halogen components and proportion.[17] **Figure 3**a shows the schematic of the vapor-phase halide-exchange of the $CsPbX_3$ films via using the directly grown $CsPbBr_3$ films to react with different HCl or HI vapors at 60 °C for certain times. Therefore, we fabricated another six kinds of $CsPbX_3$ ($CsPbCl_3$, $CsPbCl_2Br$, $CsPbClBr_2$, $CsPbBr_2I$, $CsPbBrI_2$, $CsPbI_3$) films by using the vapor-phase halide-exchange method. Figures S9 and S10 (Supporting Information) show the morphologies (a and c) and element mapping (d–f) of the resulted $CsPbCl_3$ and $CsPbI_3$ films, respectively. The atomic ratios of 1.1:1:3.05 in Figure S11a (Supporting Information) and 1.05:1:2.8 in Figure S11b (Supporting Information) accord with the $CsPbCl_3$ and $CsPbI_3$ stoichiometry, respectively. Due to the different lattice constants of three differrent perovskite, the replacement of Br into Cl or I will lead to the change of the film sizes. As shown in Figure S12 (Supporting Information), after halide-exchange procedures, the size of a film reduced from 222 µm (Br, Figure S12a, Supporting Information) to 210 µm (Cl, Figure S12b, Supporting Information) and the size of another film increase from 510 µm (Br, Figure S12c, Supporting Information) to 528 µm (I, Figure S12d, Supporting Information). Therefore, the halide-exchange procedure should be slow and careful to void the cracks in the films. Similar to the directly grown $CsPbBr_3$ monocrystalline film, the converted $CsPbCl_3$ and $CsPbI_3$ film also have angled facets, smooth surfaces, and uniformly distributed elements. The XRD spectra of

Table 1. Comparison of optical and electrical properties of $CsPbBr_3$ film with other typical monocrystalline $MAPbBr_3$ perovskite films or $CsPbBr_3$ crystals.

Material	Trap density [cm^{-3}]		Mobilities [$cm^2\ V^{-1}\ s^{-1}$]		Diffusion length [μm]		Lifetime [ns]	Mobility-lifetime product [$cm^2\ V^{-1}$]		Resistivity [GΩ cm]	Reference
	Hole	Electron	Hole	Electron	Hole	Electron		Hole	Electron		
$CsPbBr_3$ bulk crystal	1.9×10^{9}	–	2000	2300	9.5	10.9	10.5	2.1×10^{-5}	2.41×10^{-5}	–	[38]
$MAPbBr_3$ film	1.47×10^{11}	8.8×10^{10}	27.3	40.7	6.4	5.2	390	1×10^{-5}	1.59×10^{-5}	–	[42]
$MAPbBr_3$ film	–	4.8×10^{10}	–	15.7	–	–	84 000	–	1.3×10^{-3}	–	[40]
$MAPbBr_3$ film	–	1.6×10^{11}	–	59	–	1.3	242	–	1.42×10^{-5}	–	[43]
$CsPbBr_3$ bulk crystal	4.2×10^{10}	1.1×10^{10}	11	52	2.5	5.5	233	2.6×10^{-6}	1.2×10^{-5}	≈0.1	[37]
$CsPbBr_3$ film	1.8×10^{10}	1.3×10^{10}	1770	910	4.2	5.9	7.6	1.3×10^{-5}	6.9×10^{-6}	≈0.21	This work

these six perovskite films are shown in Figure 3b. Increasing the Cr content or I content leads to a continuous migration of (002)/(110) and (004)/(220) XRD peaks to higher or lower angles, respectively. These results proved the successful substitute of halogen which can also be proved in the above mentioned EDS results. For these six kinds of perovskite monocrystalline films, the peak positions locate at 414 nm (violet) for $CsPbCl_3$, 449 nm (blue) for $CsPbCl_2Br$, 491 nm (cyan) for $CsPbClBr_2$, 606 nm (yellow) for $CsPbBr_2I$, 658 nm (orange) for $CsPbBrI_2$, and 691 nm (wine) for $CsPbI_3$, respectively. (Figure 3c) Figure 3d demonstrates the absorption spectra of the six perovskite monocrystalline films which show one-to-one correspondence with PL spectra. And the optical bandgaps for $CsPbCl_3$ and $CsPbI_3$ are calculated as 2.92 and 1.8 eV, respectively (Figures S9b and S10b, Supporting Information). Figure 3e,f shows the transmission optical photographs of the real color

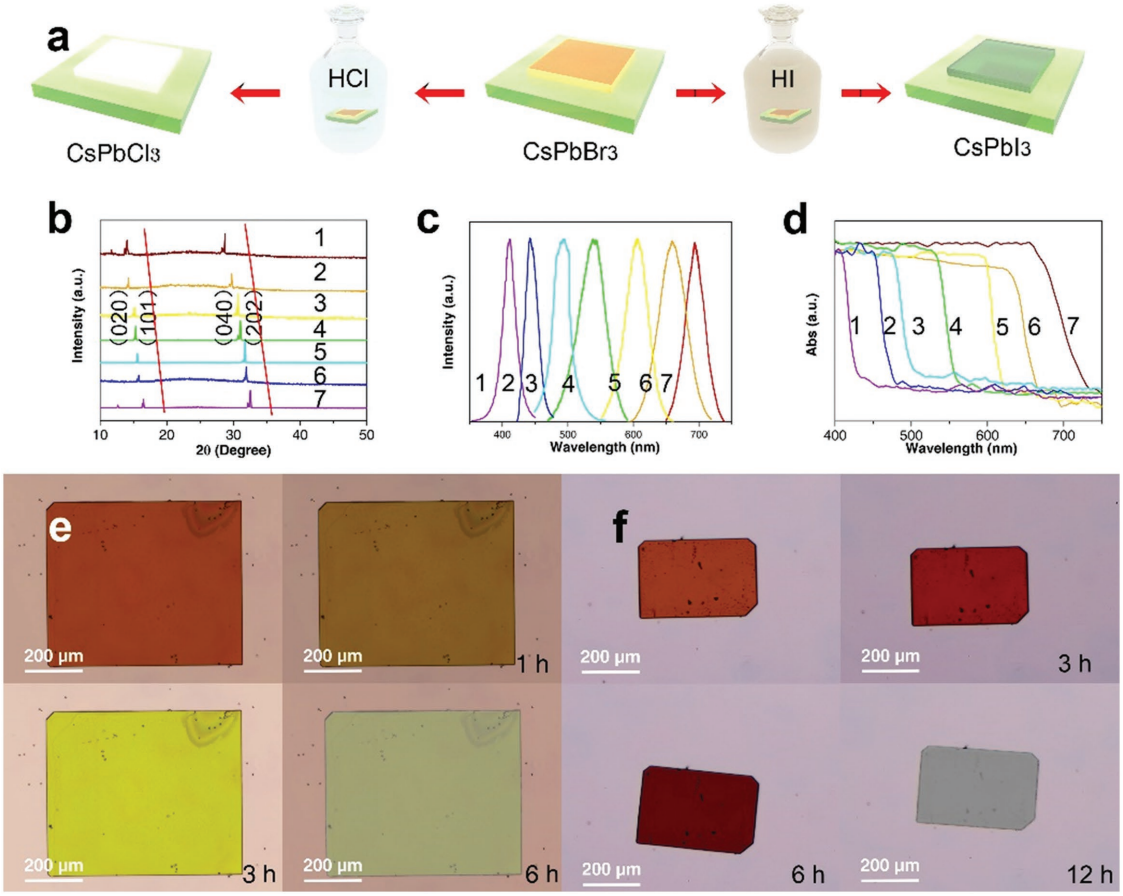

Figure 3. Multicolor perovskite films via vapor-phase halide-exchange. a) Schematic of the vapor-phase halide-exchange of the $CsPbX_3$ films along with HCl or HBr for each reaction when performed in the vapor phase. b–d) The XRD (b), PL spectra (c), and absorption spectra (d) of seven different $CsPbX_3$ (X = Cl, Br, and I) films (1–7, $CsPbCl_3$, $CsPbCl_2Br$, $CsPbClBr_2$, $CsPbBr_3$, $CsPbBr_2I$, $CsPbBrI_2$, $CsPbI_3$), showing the chemical tunability of the current films. e,f) The transmission optical photographs of the $CsPbX_3$ films showing the color change via prolonging the reaction time in HCl vapor (e) and HI vapor (f).

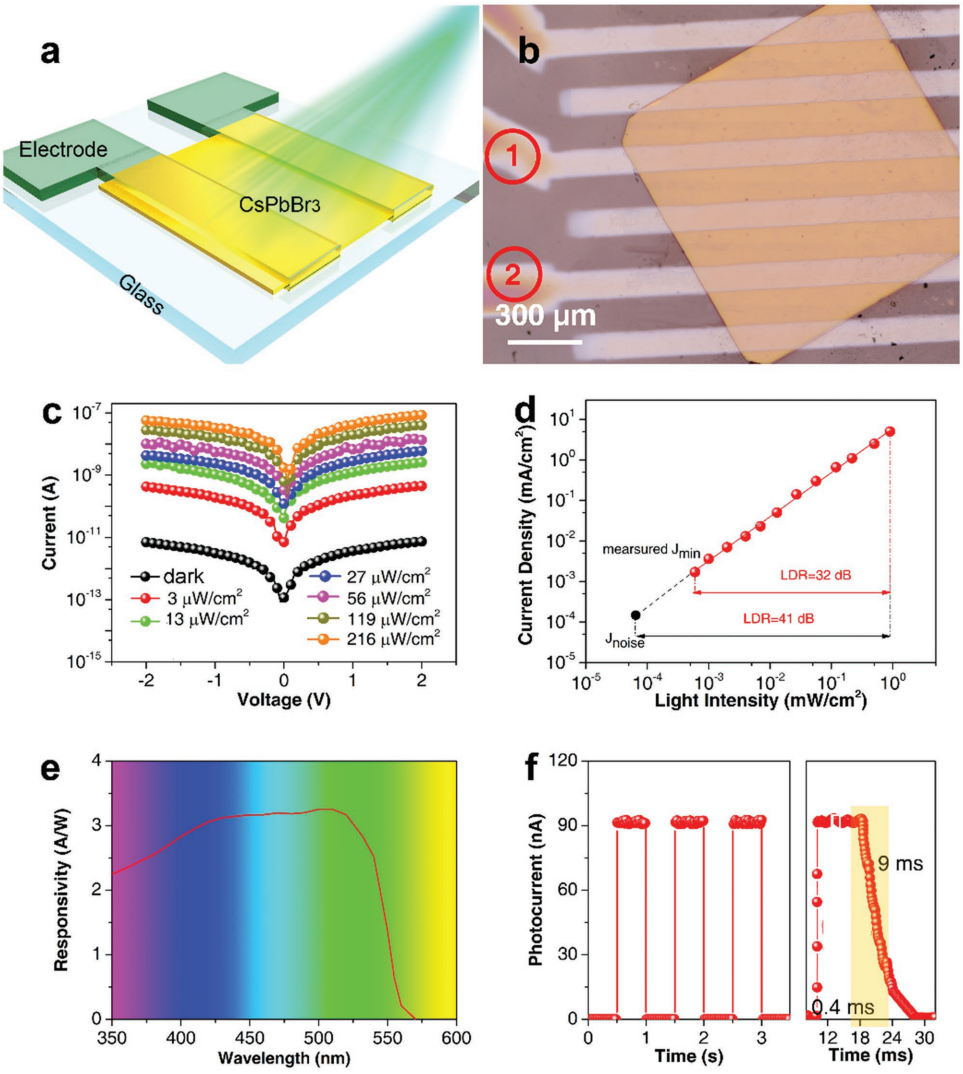

Figure 4. a) The schematic of the photodetector device structure. b) Optical image of the photodetector where electrodes 1 and 2 are used to connect to the power source. c) The *I–V* characteristics of the photodetector under 530 nm illumination with six different light intensities. d) Intensity-dependent photocurrent with a bias of 2 V. The linear dynamic range of the detector is 32 dB. e) Curve of responsivity of the photodetector as a function of light wavelength. f) Time-dependent photoresponse of the photodetector measured by periodically turning on and off a 530 nm monochromatic laser at a bias of 2 V. g) Rise time and decay time of the photodetector under 530 nm light (216 μW m^{-2}) at a bias of 2 V.

change of the $CsPbX_3$ film with different reaction time in HCl and HI vapors, respectively. The reaction rate for HI is slower than that for HCl, and it will take 12 h to transform $CsPbBr_3$ fully into $CsPbI_3$. The color of $CsPbCl_3$ is almost white while that for $CsPbI_3$ is silver gray. The HCl or HI vapor can be obtained by dissolving NaCl or KI in the concentrated H_2SO_4 or H_3PO_4 with heating, respectively. Using the concentrated hydrochloric acid as Cl source to react with the films will lead to the obvious degradation (Figure S13, Supporting Information).

Then the single $CsPbBr_3$ monocrystalline film was fabricated into photodetector. A schematic of the device structure is shown in **Figure 4**a. A layer of Au interdigital electrode (50 nm) was magnetron sputtered on top of the $CsPbBr_3$ film using a shadow mask, constructing an ohmic-type device. A 530 nm monochromatic laser was illuminated onto the film. The photograph of the device is shown in Figure S14 (Supporting Information). Figure 4b shows the optical image of the device. The size of the film used for photodetector is about 500 μm, and the thickness is 500 nm. And the electrodes 1 and 2 are linked to the positive and negative anodes of 4200 source-measure unit, respectively. Figure 4c depicts the current versus voltage (*I–V*) characteristics of the film-based device under dark condition and 530 nm light illumination (with six different light intensities), respectively. The linear relation between current and voltage demonstrates the good ohmic contact. Under 2 V bias, the dark current was only 7 pA. When the light with intensity of 216 μW cm^{-2} was turned on, the photocurrent was 97 nA at the same bias. Thus, the light on/off ratio is $>10^3$, which indicated this $CsPbBr_3$ film based device has a high light switching characteristic. As shown in Figure 4d, the photodetector exhibits broad linear response ranges from

≈10^{-4} to 1 mW cm^{-2} under a low bias of 2 V. When the signal-to-noise ratio is 1, the corresponding detection limit light intensity is 60 μW cm^{-2}. The measrued linear dynamic range (LDR) is calculated to be 32 dB while the theoretical LDR is 41 dB using the following equation

$$\mathrm{LDR} = 10 \log \frac{P_{\max}}{P_{\min}} \tag{4}$$

where $P_{\max}$ and $P_{\min}$ are the maximum and minimum values of incident light in the linear range of photocurrent, respectively.[43] The detectivity which represents the ability to detect signals is caculated to be 1.4×10^{13} cm Hz$^{0.5}$ W^{-1} according to the following equation

$$\mathrm{Detectivity} = \frac{R\sqrt{A}}{\sqrt{2GeI_{\mathrm{d}}}} \tag{5}$$

where R is the Responsivity, A is the area of the device, G is the photoconductive gain ($G = R \times E_{h\nu}$), and I_{d} is the dark current. In this work, the radius of the laser spot is ≈75 μm, which is smaller than the area between two adjacent electrodes, so the effective area of the device is 1.75×10^{-4} cm^2 since the dark current is negligible compared with the photocurrent. The spectral responsivity $R_\lambda = (J_{\mathrm{light}} - J_{\mathrm{dark}})/I_{\mathrm{light}}$ was calculated and shown in Figure 4e, where J_{light} is the photocurrent density, J_{dark} is the dark current density, and I_{light} is the incident light intensity. The photodetector exhibits a broad photoresponse range from 370 to 530 nm, showing the same trend with the absorption spectrum. It is worth knowing that the R_λ values fall in a narrow distribution of with an average value of 2.5 A W^{-1}. This relatively small responsivity may attribute the large film size since the photoinduced charge carriers can easily recombine during the transport procedure. Our photodetectors exhibit an EQE of 6.2 which was calculated from responsivity (Figure S15, Supporting Information) using the equation EQE = $Rhc/(e\lambda)$ where h is Plank's constant, c is the speed of light, e is the electronic charge, and λ is the incident light wavelength.[37,47] The periodic photoresponses of the photodetector under 530 nm monochromatic light of 216 μW cm^{-2} at 2 V show the highly stable photoresponse characteristic (left in Figure 4f). All the three cycles showed almost the same ON/OFF ratio of ≈10^3, and after each cycle, the dark current can recover to 7 pA, which is very repeatable. The rise time and decay time are confirmed to be 0.4 and 9 ms, respectively (right in Figure 4f), indicating the fast response characteristic. The periodic photoresponses under 530 nm monochromatic light with three different light intensities are shown in Figure S16 (Supporting Information). Each curve has a good repeatability and stable photocurrents. And as shown in Figure S17 (Supporting Information), the 3 dB bandwidth is 1100 Hz. The thickness of the film is one of the key parameters to influence the performance of the photodetector. So we fabricated three kinds of devices with thicknesses in the range of 0.3–1, 1–5, and 5–10 μm, respectively. All of these devices are measured at 2 V bias. As shown in Figure S18 (Supporting Information), with the increase of the film thickness, the averaged responsivity decrease obviously. This is due to the higher recombination rate and lower carriers collection efficiency.

The instability is an obstacle which handicaps the practical application of the perovskite, especially when encountering the humidity and heat. The long-term stability, which represents the film's ability to maintain their structural, optical, and electrical properties during the certain working periods, anti-humidity stability, and antithermal stability of the as-prepared $CsPbBr_3$ monocrystalline films and the resultant photodetector devices are tested. All of our $CsPbBr_3$ films and the devices are stored in the ambient environment rather than inert gases. As shown in **Figure 5**a, the $CsPbBr_3$ films suffer no obvious PL loss after being stored for two months. And the XRD intensities and peaks remain almost unchanged (Figure 5b), proving the long-term structural and chemical stability. Besides, the device exhibits high stability with little loss in responsivity after being stored in air for two months (Figure 5c), without any protection measure. The photocurrent of $CsPbBr_3$ films based device with an illumination of five continuous 30 nm laser (216 μW cm^{-2}) for 7 d almost remained the same as the initial value, and the degradation is less than 5% (Figure 5d). Then, the $CsPbBr_3$ films were stored in 90% RH air at room temperature or heated at 150 °C in 25% RH air, respectively. As shown in Figure 5e,f, no matter facing water vapor or thermal treatment, after 7 d, the morphologies of the films almost did not change and the PL loss is less than 10%. As comparison, the inorganic–organic hybrid monocrystalline perovskite $MAPbBr_3$ films were synthesized via a similar antisolvent crystallization using CH_2Cl_2 and their stability was also tested. As shown in Figure S19 (Supporting Information), when being stored in 90% RH air for 1 d, the hybrid film was seriously damaged. Besides, the operating lifetimes of the $CsPbBr_3$ film and $MAPbBr_3$ film under continuous laser irradiation were tested. Figure S20a (Supporting Information) shows the PL image of a $CsPbBr_3$ film under 325 nm laser irradiation. The PL intensity was recorded and plotted as a function of time in Figure S20b (Supporting Information), in which the $CsPbBr_3$ film shows a much longer operating time (≈5 h) than the $MAPbBr_3$ film (≈1.5 h). After 5 h irradiation, obvious degradation appeared in the film (Figure S20c, Supporting Information). Therefore, our $CsPbBr_3$ films show much stronger practicability compared with the hybrid counterparts. However, when stored in the saturated steam heated at 80 °C, the films show obvious degradation in less than 1 d, which is shown in Figure S21 (Supporting Information). This is due to the liquid water forms on the films and dissolves the CsBr, leading to the destruction of the crystal structure. This might be improved by hydrophobic treatment of the film's surface. In brief, our $CsPbBr_3$ monocrystalline films demonstrate excellent stability and may replace the hybrid counterparts in the future.

In conclusion, a space-limited and substrate-independent antisolvent vapor-assisted crystallization growth is demonstrated for mm-level large $CsPbBr_3$ monocrystalline films. The films have comparable quality to bulk single crystals. The halide constituent of the prepared monocrystalline films can be easily tuned via a vapor-phase halide-exchange method. The film-based photodetectors show a fast, sensitive, and repeatable photoresponse characteristics. Moreover, an excellent long-term stability toward humidity and thermal treatment is shown. These results might broaden the applications of the high-performance optoelectronic devices.

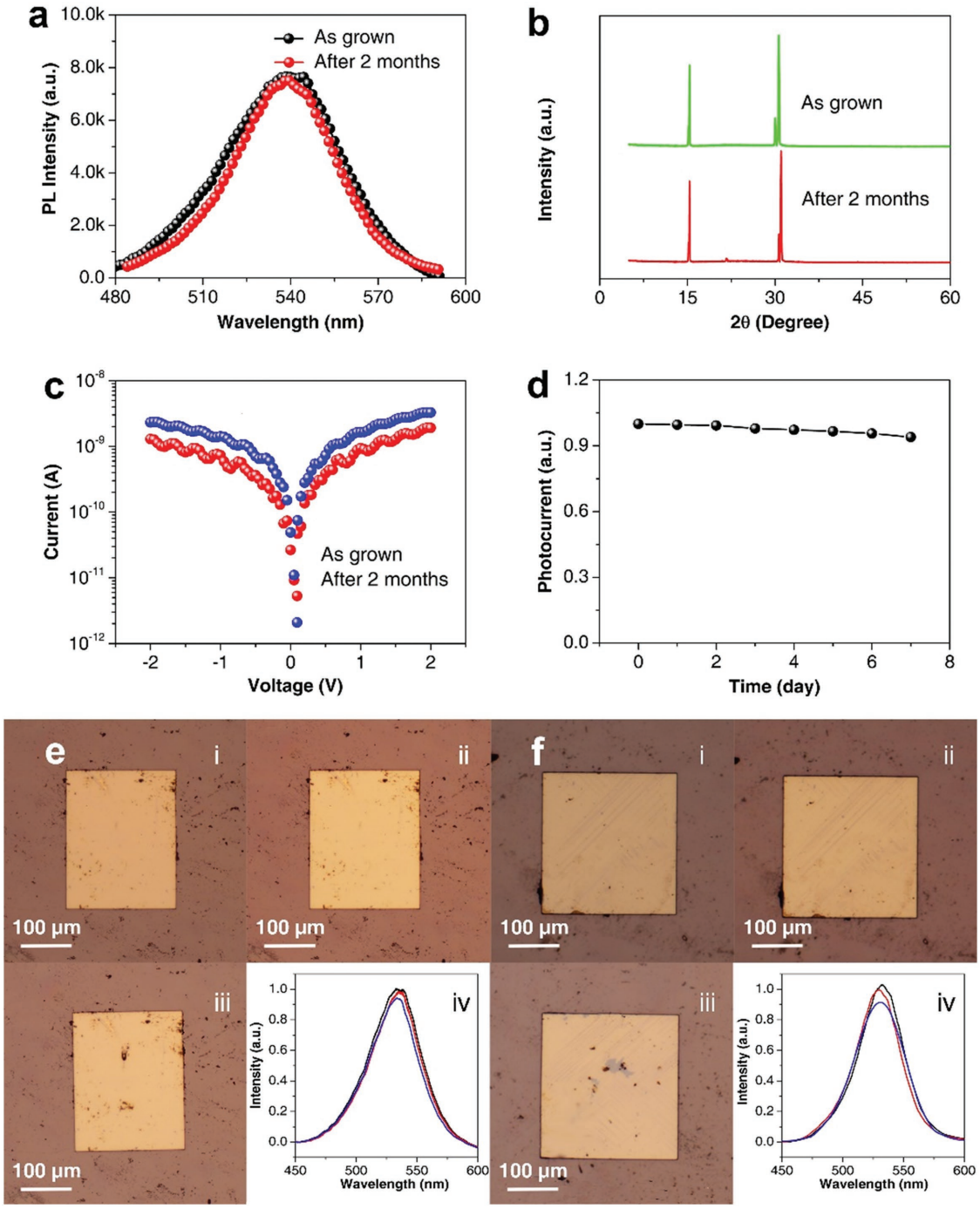

Figure 5. The long-term stability of the $CsPbBr_3$ films and the photodetector device. a) PL spectra and b) XRD spectra of the as-grown $CsPbBr_3$ films and the films which had been stored in the ambient environment for two months. c) The *I–V* curves of the as-grown $CsPbBr_3$ film fabricated photodetector and the same device stored in air for two months under 510 nm illumination with a light intensity of 13 μW cm^{-1}, which demonstrate the good air stability of the devices. d) Normalized photocurrent of $CsPbBr_3$ photodetectors under a 510 nm laser with the light intensity of 216 μW for 7 d. The stability of the $CsPbBr_3$ films toward humidity. e) (i)–(iii) The optical images of a same $CsPbBr_3$ film before and after being stored in the 90 RH% air for 1 and 7 d, which show no obvious morphological changes. (iv) The corresponding PL spectra. The thermal stability of the $CsPbBr_3$ films. f) (i)–(iii) The optical images of a same $CsPbBr_3$ film before and after being heated at 150 °C in the ambient environment for 1 and 7 d, which show no obvious morphological changes. (iv) The corresponding PL spectra.

Experimental Section

Chemicals and Reagents: Methylammonium bromide (CH_3NH_2Br), cesium bromide (CsBr), and lead bromide ($PbBr_2$, ≥98%) were purchased from Xi'an Polymer Light Technology Corp. DMSO (anhydrous, ≥99.9%), MeCN (anhydrous, ≥99.9%), DMF (anhydrous, ≥99.9%), and dichloromethane were purchased from Sigma-Aldrich. Sodium chloride and potassium iodide were purchased from Aladdin.

All chemicals were used as received without any further purification.

Preparation of Substrates: The 2.5 × 2.5 cm ⟨100⟩ silicon wafer, glass, and Si/SiO_2 substrates were successively cleaned with water, ethanol, and acetone in an ultrasonic bath for 15 min. All the substrates were treated by an oxygen plasma cleaner at 300 W for 600 s. PEN substrates were used without further treatment after removing the protecting films.

$CsPbBr_3$ Synthesis: A stock solution of CsBr and $PbBr_2$ mixture dissolved in DMSO was spread on the hydrophilic SiO_2/Si, glass, or PEN substrate. The precursor solution preparation can be seen in a reported literature.[12] In brief, 0.4 M CsBr and $PbBr_2$ were simultaneously dissolved in DMSO at 50 °C. Then the solution was saturated with MeCN dropwise under vigorous stirring and stirred for 24 h at 50 °C. Finally, the solution was filtered with filters. Then another hydrophobic substrate was brought into contact with the DMSO solution and two clean flat substrates were clipped together. A few seconds vacuum pumping was conducted to eliminate the bubbles. And a pressure (≈200 kPa) was applied uniformly on the two substrates. Then they were placed in a glass beaker which contained MeCN. The perovskite films would gradually grow on the hydrophilic substrates with the MeCN diffusion into the DMSO.

$MAPbBr_3$ Synthesis: 1.1 M MABr and $PbBr_2$ were simultaneously dissolved in DMF at 50 °C. A stock solution of the mixture was spread on the hydrophilic SiO_2/Si substrate. Then another hydrophobic substrate was brought into contact with the DMF solution and two clean flat substrates were clipped together. A few seconds vacuum pumping was conducted to eliminate the bubbles. And a pressure (≈200 kPa) was applied uniformly on the two substrates. Then they were placed in a glass beaker which contained CH_2Cl_2.

Vapor-Phase Halide-Exchange: The HCl vapor was obtained by dissolving NaCl in concentrated H_2SO_4 while the HI vapor was obtained by dissolving KI in concentrated H_3PO_4. Then the $CsPbBr_3$ films grown on the glass substrate were put into the obtained vapor and heated at 60 °C for certain time. It will take 1, 3, and 6 h to obtain $CsPbClBr_2$, $CsPbCl_2Br$, and $CsPbCl_3$, respectively. For $CsPbBr_2I$, $CsPbBrI_2$, and $CsPbI_3$, the corresponding time is 3, 6, and 12 h.

Characterization: Morphologies of the films were characterized using an optical microscope (Zeiss Observer Z1) and SEM (Hitachi SU8020). Crystallinity of the films was determined by XRD (PANalytical X'Pert3). The crystallinity of the film was confirmed using a JEM-TEM-2100F operating at a 200 kV accelerating voltage. The perovskite films were transferred onto copper grid through a dry transfer technique.[48] The absorption spectra were obtained by an UV–vis–NIR spectrophotometer (Shimadzu UV 3600). The PL spectra were detected by Laser Confocal Micro-Raman system (LabRAM HR Evolution). The decay curve of transient state PL was determined by steady-state/transient fluorescence spectrometer (FLS980).

Device Fabrication and Electrical Characterization: A layer of Au interdigital electrode (50 nm) was magnetron sputtered (Kurt J. Lesker PVD75) on top of the $CsPbBr_3$ film using a shadow mask, constructing an ohmic-type device. The monochromatic light was outputted by a laser, and the light intensity was controlled by changing the current (WhiteLase SC400), and the specific intensities were measured by an optical power meter. The *I–V* curves were recorded by a Keithley 4200 source-measure unit. And the photoresponse current was measured by a voltage testing system (NI PXI-2530). An optical chopper was placed between the laser and the devices to modulate the continuous wave laser beam. The hole-only device ($Au/Ti/CsPbBr_3/Ti/Au$) and electron-only device ($Au/CsPbBr_3/Au$) were prepared by growing the films onto the 30 nm Au or 30 nm Au/10 nm Ti electrode and depositing 30 nm Au or 30 nm Au/10 nm Ti electrode on the surface of the films, respectively.

Supporting Information

Supporting Information is available from the Wiley Online Library or from the author.

Acknowledgements

The authors thank the support from the support of National Key R&D project from Minister of Science and Technology, China (2016YFA0202703), National Natural Science Foundation of China (Nos. 51622205, 61675027, 51432005, 61505010, and 51502018), Beijing City Committee of Science and Technology (Z171100002017019), Beijing Natural Science Foundation (4181004, 4182080, 4184110, and 2184131), and the "Thousand Talents" program of China for pioneering researchers and innovative teams.

Conflict of Interest

The authors declare no conflict of interest.

Keywords

$CsPbBr_3$, monocrystalline films, photodetectors, stability

Received: April 2, 2018
Revised: August 4, 2018
Published online:

[1] W. Chen, Y. Wu, Y. Yue, J. Liu, W. Zhang, X. Yang, H. Chen, E. Bi, I. Ashraful, M. Graetzel, L. Han, *Science* **2015**, *350*, 944.
[2] W. Nie, H. Tsai, R. Asadpour, J. C. Blancon, A. J. Neukirch, G. Gupta, J. J. Crochet, M. Chhowalla, S. Tretiak, M. A. Alam, H. L. Wang, A. D. Mohite, *Science* **2015**, *347*, 522.
[3] D. Shi, V. Adinolfi, R. Comin, M. Yuan, E. Alarousu, A. Buin, Y. Chen, S. Hoogland, A. Rothenberger, K. Katsiev, Y. Losovyj, X. Zhang, P. A. Dowben, O. F. Mohammed, E. H. Sargent, O. M. Bakr, *Science* **2015**, *347*, 519.
[4] H. Lu, K. Deng, N. Yan, Y. Ma, B. Gu, Y. Wang, L. Li, *Sci. Bull.* **2016**, *61*, 778.
[5] G. Hu, W. Guo, R. Yu, X. Yang, R. Zhou, C. Pan, Z. L. Wang, *Nano Energy* **2016**, *23*, 27.
[6] Q. Dong, Y. Fang, Y. Shao, P. Mulligan, J. Qiu, L. Cao, J. Huang, *Science* **2015**, *347*, 967.
[7] Y. Ling, Z. Yuan, Y. Tian, X. Wang, J. C. Wang, Y. Xin, K. Hanson, B. Ma, H. Gao, *Adv. Mater.* **2016**, *28*, 305.
[8] J. Byun, H. Cho, C. Wolf, M. Jang, A. Sadhanala, R. H. Friend, H. Yang, T. W. Lee, *Adv. Mater.* **2016**, *28*, 7515.
[9] X. Gong, Z. Yang, G. Walters, R. Comin, Z. Ning, E. Beauregard, V. Adinolfi, O. Voznyy, E. H. Sargent, *Nat. Photonics* **2016**, *10*, 253.
[10] N. Wang, L. Cheng, R. Ge, S. Zhang, Y. Miao, W. Zou, C. Yi, Y. Sun, Y. Cao, R. Yang, Y. Wei, Q. Guo, Y. Ke, M. Yu, Y. Jin, Y. Liu, Q. Ding, D. Di, L. Yang, G. Xing, H. Tian, C. Jin, F. Gao, R. H. Friend, J. Wang, W. Huang, *Nat. Photonics* **2016**, *10*, 699.
[11] A. L. Rogach, *Sci. Bull.* **2017**, *62*, 314.
[12] S. Chen, K. Roh, J. Lee, W. K. Chong, Y. Lu, N. Mathews, T. C. Sum, A. Nurmikko, *ACS Nano* **2016**, *10*, 3959.
[13] S. Chen, C. Zhang, J. Lee, J. Han, A. Nurmikko, *Adv. Mater.* **2017**, *29*, 1604781.
[14] J. Feng, X. Yan, Y. Zhang, X. Wang, Y. Wu, B. Su, H. Fu, L. Jiang, *Adv. Mater.* **2016**, *28*, 3732.
[15] P. Liu, X. He, J. Ren, Q. Liao, J. Yao, H. Fu, *ACS Nano* **2017**, *11*, 5766.
[16] M. Saliba, S. M. Wood, J. B. Patel, P. K. Nayak, J. Huang, J. A. Alexander-Webber, B. Wenger, S. D. Stranks, M. T. Hoerantner, J. T. W. Wang, R. J. Nicholas, L. M. Herz, M. B. Johnston, S. M. Morris, H. J. Snaith, M. K. Riede, *Adv. Mater.* **2016**, *28*, 923.

[17] X. He, P. Liu, H. Zhang, Q. Liao, J. Yao, H. Fu, *Adv. Mater.* **2017**, *29*, 1604510.
[18] R. Dong, Y. Fang, J. Chae, J. Dai, Z. Xiao, Q. Dong, Y. Yuan, A. Centrone, X. C. Zeng, J. Huang, *Adv. Mater.* **2015**, *27*, 1912.
[19] Y. Fang, Q. Dong, Y. Shao, Y. Yuan, J. Huang, *Nat. Photonics* **2015**, *9*, 679.
[20] Y. Lee, J. Kwon, E. Hwang, C. H. Ra, W. J. Yoo, J. H. Ahn, J. H. Park, J. H. Cho, *Adv. Mater.* **2015**, *27*, 41.
[21] M. I. Saidaminov, V. Adinolfi, R. Comin, A. L. Abdelhady, W. Peng, I. Dursun, M. Yuan, S. Hoogland, E. H. Sargent, O. M. Bakr, *Nat. Commun.* **2015**, *6*, 8724.
[22] P. Gui, Z. Chen, B. Li, F. Yao, X. Zheng, Q. Lin, G. Fang, *ACS Photonics* **2018**, *5*, 2113.
[23] H. Zeng, G. Duan, Y. Li, S. Yang, X. Xu, W. Cai, *Adv. Funct. Mater.* **2010**, *20*, 561.
[24] C. Pan, J. Zhu, *J. Mater. Chem.* **2009**, *19*, 869.
[25] W. Guo, C. Xu, G. Zhu, C. Pan, C. Lin, Z. L. Wang, *Nano Energy* **2012**, *1*, 176.
[26] C. Wang, R. Ba, K. Zhao, T. Zhang, L. Dong, C. Pan, *Nano Energy* **2015**, *14*, 364.
[27] Q. Hua, J. Sun, H. Liu, R. Bao, R. Yu, J. Zhai, C. Pan, Z. L. Wang, *Nat. Commun.* **2018**, *9*, 244.
[28] X. Wang, Y. Zhang, X. Zhang, Z. Huo, X. Li, M. Que, Z. Peng, H. Wang, C. Pan, *Adv. Mater.* **2017**, 1706738.
[29] G. Gao, B. Wan, X. Liu, Q. Sun, X. Yang, L. Wang, C. Pan, Z. L. Wang, *Adv. Mater.* **2018**, 1705088.
[30] S. A. Veldhuis, P. P. Boix, N. Yantara, M. Li, T. C. Sum, N. Mathews, S. G. Mhaisalkar, *Adv. Mater.* **2016**, *28*, 6804.
[31] Y. Zhao, K. Zhu, *Chem. Soc. Rev.* **2016**, *45*, 655.
[32] A. Waleed, Z. Fan, *Sci. Bull.* **2017**, *62*, 645.
[33] D. P. McMeekin, G. Sadoughi, W. Rehman, G. E. Eperon, M. Saliba, M. T. Hoerantner, A. Haghighirad, N. Sakai, L. Korte, B. Rech, M. B. Johnston, L. M. Herz, H. J. Snaith, *Science* **2016**, *351*, 151.
[34] Y. Fu, H. Zhu, C. C. Stoumpos, Q. Ding, J. Wang, M. G. Kanatzidis, X. Zhu, S. Jin, *ACS Nano* **2016**, *10*, 7963.
[35] M. Kulbak, S. Gupta, N. Kedem, I. Levine, T. Bendikov, G. Hodes, D. Cahen, *J. Phys. Chem. Lett.* **2016**, *7*, 167.
[36] D. N. Dirin, I. Cherniukh, S. Yakunin, Y. Shynkarenko, M. V. Kovalenko, *Chem. Mater.* **2016**, *28*, 8470.
[37] M. I. Saidaminov, M. A. Haque, J. Almutlaq, S. Sarmah, X. H. Miao, R. Begum, A. A. Zhumekenov, I. Dursun, N. Cho, B. Murali, O. F. Mohammed, T. Wu, O. M. Bakr, *Adv. Opt. Mater.* **2017**, *5*, 8470.
[38] J. Song, Q. Cui, J. Li, J. Xu, Y. Wang, L. Xu, J. Xue, Y. Dong, T. Tian, H. Sun, H. Zeng, *Adv. Opt. Mater.* **2017**, *5*, 1700157.
[39] Y. Rakita, N. Kedem, S. Gupta, A. Sadhanala, V. Kalchenko, M. L. Bohm, M. Kulbak, R. H. Friend, D. Cahen, G. Hodes, *Cryst. Growth Des.* **2016**, *16*, 5717.
[40] Y. X. Chen, Q. Q. Ge, Y. Shi, J. Liu, D. J. Xue, J. Y. Ma, J. Ding, H. J. Yang, J. S. Hu, L. J. Wan, *J. Am. Chem. Soc.* **2016**, *138*, 16196.
[41] W. Peng, L. Wang, B. Murali, K. T. Ho, A. Bera, N. Cho, C. F. Kang, V. M. Burlakov, J. Pan, L. Sinatra, C. Ma, W. Xu, D. Shi, E. Alarousu, A. Goriely, J. H. He, O. F. Mohammed, T. Wu, O. M. Bakr, *Adv. Mater.* **2016**, *28*, 3383.
[42] H. S. Rao, W. G. Li, B. X. Chen, D. B. Kuang, C. Y. Su, *Adv. Mater.* **2017**, *29*, 1602639.
[43] Z. Yang, Y. Deng, X. Zhang, S. Wang, H. Chen, S. Yang, J. Khurgin, N. X. Fang, X. Zhang, R. Ma, *Adv. Mater.* **2018**, *30*, 1704333.
[44] S. Wang, K. Wang, Z. Gu, Y. Wang, C. Huang, N. Yi, S. Xiao, Q. Song, *Adv. Opt. Mater.* **2017**, *5*, 1700023.
[45] Z. Dang, J. Shamsi, F. Palazon, M. Imran, Q. A. Akkerman, S. Park, G. Bertoni, M. Prato, R. Brescia, L. Manna, *ACS Nano* **2017**, *11*, 2124.
[46] X. Hu, H. Zhou, Z. Jiang, X. Wang, S. Yuan, J. Lan, Y. Fu, X. Zhang, W. Zheng, X. Wang, X. Zhu, L. Liao, G. Xu, S. Jin, A. Pan, *ACS Nano* **2017**, *10*, 9869.
[47] L. Hu, J. Yan, M. Liao, L. Wu, X. Fang, *Small* **2011**, *7*, 1012.
[48] C. Huo, X. Liu, X. Song, Z. Wang, H. Zeng, *J. Phys. Chem. Lett.* **2017**, *8*, 4785.

